

RESEARCH ARTICLE

10.1002/2015JC011054

Key Points:

- Significant seasonal variability of EKE in the western tropical Pacific
- Barotropic instability controls the seasonal cycle of EKE
- Variation of meander of the NECC results in the EKE variations

Correspondence to:

Y. Du,
duyan@scsio.ac.cn

Citation:

Chen, X., B. Qiu, S. Chen, Y. Qi, and Y. Du (2015), Seasonal eddy kinetic energy modulations along the North Equatorial Countercurrent in the western Pacific, *J. Geophys. Res. Oceans*, 120, 6351–6362, doi:10.1002/2015JC011054.

Received 17 JUN 2015

Accepted 3 SEP 2015

Accepted article online 4 SEP 2015

Published online 20 SEP 2015

Seasonal eddy kinetic energy modulations along the North Equatorial Countercurrent in the western Pacific

Xiao Chen^{1,2,3}, Bo Qiu³, Shuiming Chen³, Yiquan Qi¹, and Yan Du¹
¹State Key Laboratory of Tropical Oceanography, South China Sea Institute of Oceanology, Chinese Academy of Sciences, Guangzhou, China, ²University of Chinese Academy of Sciences, Beijing, China, ³Department of Oceanography, University of Hawaii at Manoa, Honolulu, Hawaii, USA

Abstract Seasonal eddy kinetic energy (EKE) variability and its associated eddy energy conversion processes in the western tropical Pacific are investigated using satellite altimeter observations and a global, eddy-resolving, ocean general circulation model (OGCM). Both the altimeter-observed sea surface height anomalies and the OGCM simulation show an area with enhanced EKE east of the Mindanao Island centered around 133°E and 5°N. This enhanced EKE area corresponds to the location of the quasi-stationary meander of the North Equatorial Countercurrent (NECC) and is bordered to the south by the Halmahera Eddy. The mesoscale EKE in this area exhibits a clear seasonality, strong in summer (July–August) and weak in winter (November–January), and much of this seasonality is confined to the upper 200 m layer. An investigation into the upper ocean eddy energetics based on the OGCM simulation reveals that the areal barotropic eddy energy conversion rate has an annual cycle similar to the EKE variations, while the areal baroclinic eddy energy conversion is found to be much smaller than the barotropic conversion rate and exhibits no clear seasonal changes. This indicates that the EKE variations are largely controlled by barotropic conversion of the seasonally varying regional circulation. By examining the seasonal background circulation changes, we find that the amplification of the barotropic eddy energy conversion rate in July–August is related to the seasonal evolution of the Mindanao Current and the New Guinea Coastal Current that amplifies the curvature and amplitude of the quasi-stationary meander of the NECC and results in an elevated EKE level through increased regional barotropic conversion.

1. Introduction

The low-latitude northwestern Pacific is a region of complex ocean circulation characterized by current confluences, bifurcations, and retroflexions (see Figure 1). In its climatological mean state, the North Equatorial Current (NEC) flows westward, carrying wind-driven convergent Sverdrup transport across the interior Pacific. The surface NEC bifurcates near 12°N along the Philippine coast to form the northward Kuroshio and the southward Mindanao Current (MC) [e.g., Nitani, 1972; Qiu and Chen, 2010, and references therein]. Existing in the wind-driven North Pacific tropical gyre, the MC is an important western boundary current, transporting subtropical-origin North Pacific water equatorward. At the southern tip of the Mindanao Island at ~5°N, one portion of the MC intrudes into the Celebes Sea and feeds the Indonesian Throughflow (ITF); the remaining portion of the MC veers eastward to form the North Equatorial Countercurrent (NECC) [e.g., Lukas et al., 1991; Gordon and Fine, 1996; Kashino et al., 2001].

East of the Halmahera Island near 128°E, the eastward-flowing NECC is strengthened by inflows from the New Guinea Coastal Current (NGCC) and the South Equatorial Current (SEC), both of which carry the surface Southern Hemisphere-origin water across the equator and toward the eastern equatorial Pacific [e.g., Lukas et al., 1991; Hsin and Qiu, 2012a,b; Kashino et al., 2013]. Southeast of the Mindanao Island, the NECC is known to exhibit a stationary meander that is accompanied by two permanent recirculation eddies: the cyclonic Mindanao Eddy (ME) centered around 128°E, 7.5°N and the anticyclonic Halmahera Eddy (HE) centered around 131°E, 3°N [e.g., Masumoto and Yamagata, 1991; Qiu and Lukas, 1996; Heron et al., 2006].

Subject to the regional monsoonal wind forcing, as well as influences from the remotely forced anomalies propagated from the interior tropical Pacific, the low-latitude North Pacific western boundary circulation

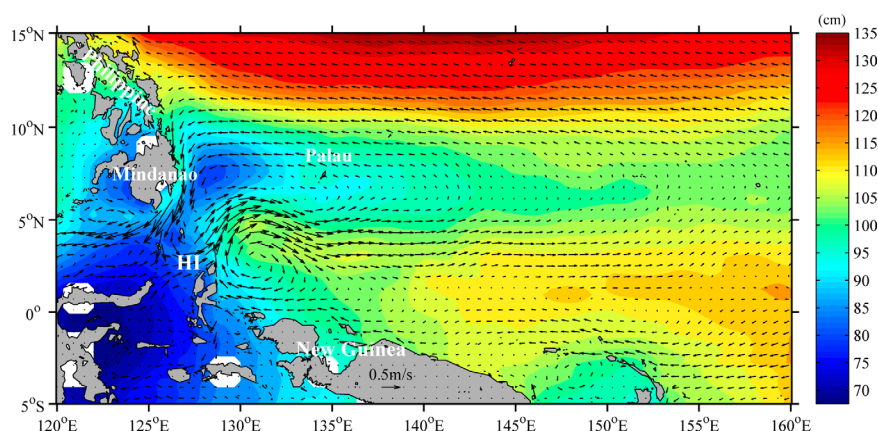


Figure 1. Mean sea surface height (colors) in the western Pacific based on satellite altimetry observations (AVISO). The black arrows indicate the mean surface currents from the OFES QSCAT run. Both results are averaged from July 1999 to October 2009. Here HI stands for Halmahera Island.

described above undergoes strong seasonal fluctuations. For example, using data of hydrography and sea level records at islands, Wyrski and Kendall [1967] and Wyrski [1974] observed that the strength of both NEC and NECC is strong (weak) in summer/fall (winter/spring). Similar seasonality of the NEC and NECC strength is detected and documented by Reverdin *et al.* [1994], Qiu and Joyce [1992], and Heron *et al.* [2006], and it is accompanied by the seasonal latitudinal migration of the NEC, shifting northward (southward) in summer/fall (winter/spring) [e.g., Qiu and Lukas, 1996; Kim *et al.*, 2004; Chen and Wu, 2011]. Based on moored current meter observations and numerical model simulations, the MC has been detected to strengthen in summer and weaken in winter [e.g., Kashino *et al.* 2005; Tozuka *et al.*, 2002]. Along the New Guinea coast, the NGCC has also been observed to intensify in boreal summer and weaken, or reverse its direction, in boreal winter [Ueki *et al.*, 2003]. In close connection with the seasonal NGCC variation, the HE has been detected to

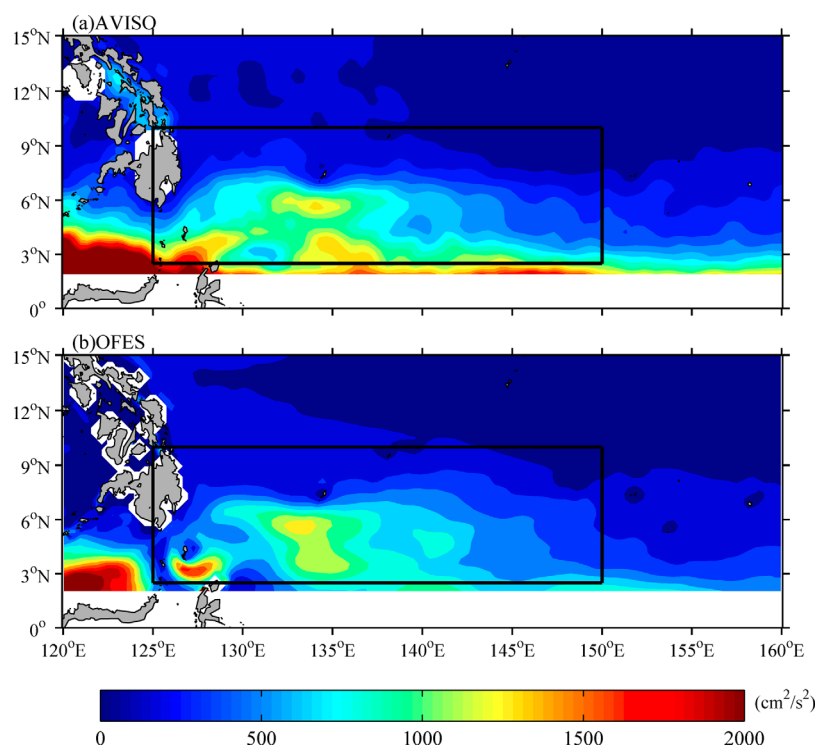


Figure 2. Eddy kinetic energy distributions calculated from the sea surface height anomalies of (a) AVISO and (b) QSCAT run. In deriving (b), the QSCAT run data were mapped onto the same horizontal grid as the AVISO. Black box indicates the area in which the EKE time series and budget are calculated.

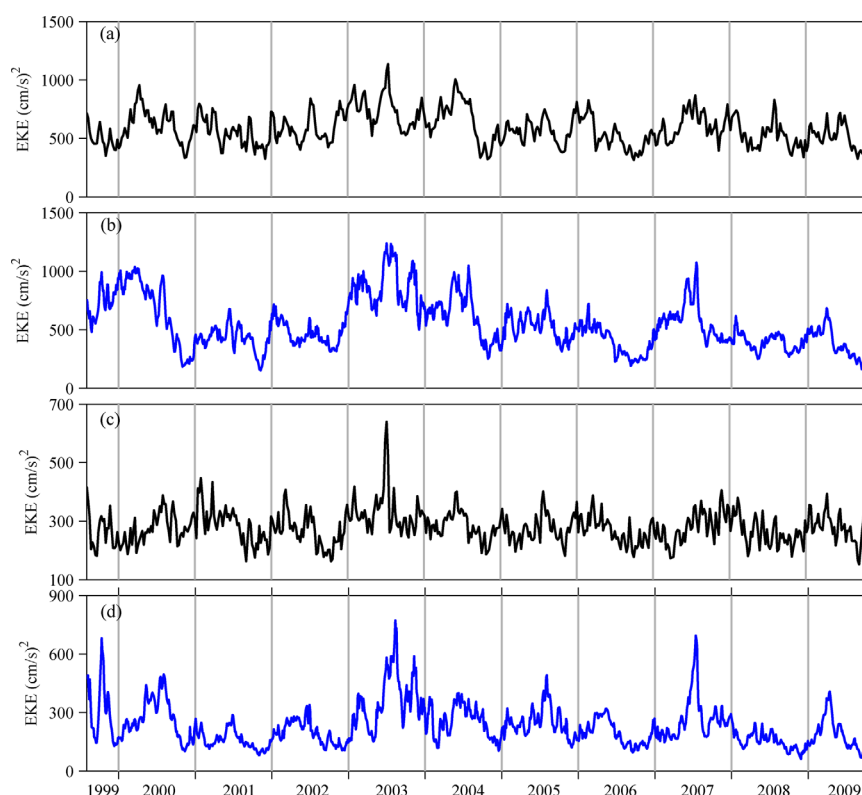


Figure 3. EKE time series calculated from the SSH anomalies from (a) AVISO and (b) QSCAT run in the region of 125°E–150°E, 2.5°N–10°N. Here the QSCAT run SSH data are remapped to the AVISO grid. The two time series have a correlation coefficient of 0.63. (c) EKE time series calculated from the 150 day high-pass filtered AVISO SSH anomalies. (d) Same as Figure 3c except from the 150 day high-pass filtered QSCAT run SSH anomalies. The correlation between (c) and (d) is 0.46.

migrate northwestward in boreal summer and southeastward in boreal winter [e.g., Heron *et al.*, 2006; Kashino *et al.*, 2013]. Dynamically, much of the seasonal circulation variability has been demonstrated to be induced by the seasonal evolution of the regional monsoonal winds being northeasterly in winter (December–March) versus southwesterly in summer (June–September).

While previous investigations have focused on the dynamical processes leading to the seasonal variability of the regional circulation (e.g., the relative importance of the local wind forcing versus the remote wind forcing), less attention has been paid to how these seasonal circulation changes can impact on the regional mesoscale eddy variability. As the regional flow field changes on the seasonal time scale, the horizontal velocity shear, the thermocline depth, and the meandering path/curvature will all fluctuate. This could modify the stability properties of the regional circulation, affecting potentially the generation of mesoscale eddies. To explore this modification, we combine in this study observational data from satellite altimeters and the output of a global eddy-resolving ocean general circulation model (OGCM) simulation. The objectives are to detect the eddy modulations in the low-latitude northwestern Pacific and to clarify their dynamical processes on the seasonal time scale.

2. Data and Methods

2.1. Observational Data

In this study, we use the merged sea surface height (SSH) anomaly data distributed by AVISO (Archiving Validation and Interpretation of Satellite Data in Oceanography; <http://www.aviso.oceanobs.com/>) that combines simultaneous measurements from two satellite altimeters (TOPEX/Poseidon or Jason-1 and ERS or Envisat). It has a $1/3^\circ \times 1/3^\circ$ spatial resolution and a weekly time interval. More detailed information about the data quality analysis and mapping method can be found in Le Traon and Ogor [1998] and Le Traon *et al.* [1998]. To synchronize with the time period of the model simulation, the AVISO SSH anomaly from July

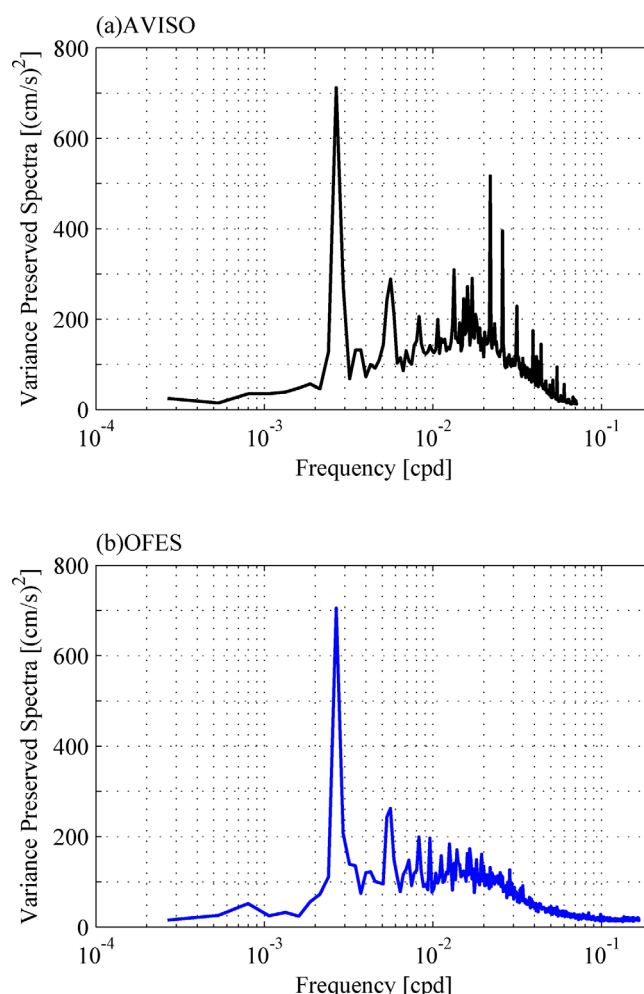


Figure 4. Variance-preserved power spectra as a function of frequency of the surface zonal and meridional geostrophic velocity anomalies in the area of 125°E–150°E, 2.5°N–10°N: (a) AVISO and (b) QSCAT run. Frequency unit cpd stands for cycle per day.

and 54 vertical levels. The time interval for the model archive is 3 days spanning from 22 July 1999 to 30 October 2009. In the following analyses, we use the QSCAT run output exclusively.

3. Verification of Model Simulation

Before exploring the dynamical processes governing the EKE signals in the QSCAT run output, it is important to quantify the veracity of the QSCAT simulation against the available satellite altimetry measurements. To do so, we compare in Figure 2 the time-mean surface EKE distributions in the tropical northwestern Pacific calculated from the SSH anomalies from the satellite observations versus those from the QSCAT simulation. In deriving Figure 2b, we have mapped the QSCAT run SSH anomaly data onto the same horizontal grid as the AVISO product and the time mean is taken from 22 July 1999 to 30 October 2009. Both the AVISO and the QSCAT simulation show that outside the Celebes Sea, elevated EKE values appear in the region bounded by 125°E–150°E and 2.5°N–10°N within which the NECC and HE are located (see black box in Figure 2). The simulated and observed EKE signals in Figure 2 have similar amplitudes and, by and large, they agree with geographical distributions; for example, both maps indicate a localized EKE maximum south-southwest off the Palau Island at 134.5°E and 7.5°N.

Figures 3a and 3b compare the observed and simulated time series of EKE averaged in the area of 125°E–150°E and 2.5°N–10°N. Overall, the two time series exhibit visually similar seasonal and interannual

1999 to October 2009 is used. From the gridded SSH anomaly data $h'(x, y, t)$, surface eddy kinetic energy (EKE) can be readily calculated by:

$$EKE \equiv \frac{g^2}{2f^2} \left[\left(\frac{\partial h'}{\partial x} \right)^2 + \left(\frac{\partial h'}{\partial y} \right)^2 \right] \quad (1)$$

where g is the gravity constant and f is the Coriolis parameter.

2.2. Model Data

Output from an eddy-resolving model, the OGCM for the Earth Simulator (OFES), is used in this study [Masumoto *et al.*, 2004; Sasaki *et al.*, 2008]. Based on Modular Ocean Model (MOM3), the quasi-global OFES model has three simulations (CLIM, NCEP, and QSCAT runs). The CLIM run is initialized from rest with the World Ocean Atlas 1998 (WOA98) [Boyer and Levitus, 1997] and is spun-up with the climatological monthly forcing from the National Centers for Environmental Prediction/National Center for Atmospheric Research (NCEP/NCAR) reanalysis [Kalnay *et al.*, 1996] for 50 years. After the 50 year spin-up integration, the daily atmospheric forcing of the NCEP/NCAR reanalysis is used to force the model from 1950 (the NCEP run). The QSCAT run uses the NCEP run output of 20 July 1999 as its initial condition and is forced subsequently by the wind stress data from the QuikSCAT measurements. The QSCAT run output has a $0.1^\circ \times 0.1^\circ$ horizontal resolution

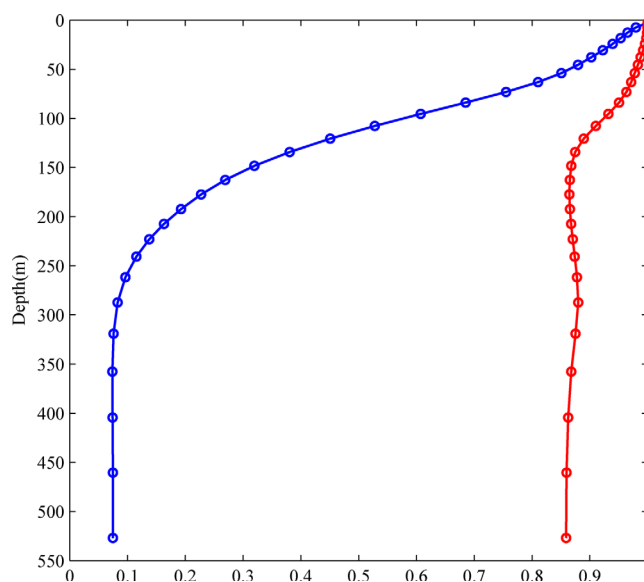


Figure 5. Blue line: EKE averaged in 125°E–150°E, 2.5°N–10°N as a function of depth from the QSCAT run; the EKE level has been normalized by its surface value: $\langle E(t, z) \rangle / \langle E(t, 0) \rangle$. Red line: EKE coherence level as a function of depth with respect to the surface EKE signals; see equation (3) for the definition of coherence level.

5.48×10^{-3} cpd; cpd: cycle per day), significant eddy variability exists in the 30–100 day band (frequency = $1.0\text{--}3.3 \times 10^{-2}$ cpd) clearly. The 30–100 day band represents the intraseasonal SSH signals associated with the mesoscale circulation fluctuations. To better focus on the mesoscale variability in this frequency band, we divide the SSH anomaly signal h' into:

$$h'(x, y, t) = \tilde{h}(x, y, t) + h''(x, y, t) \quad (2)$$

where \tilde{h} and h'' denote the h' signals with time scales longer and shorter than 150 days, respectively. In Figures 3c and 3d, we plot the EKE time series in 125°E–150°E and 2.5°N–10°N using the high-pass filtered h'' time series of AVISO and the QSCAT run. In comparison with the EKE time series based on the original SSH time series (i.e., Figures 3a and 3b), the energy level becomes lower. However, by excluding the low-frequency circulation variability with periods longer than 150 days, the seasonal modulation by the mesoscale circulation fluctuations becomes more regular and prominent in both time series of Figures 3c and 3d.

4. Seasonal EKE Modulation Along the NECC

To explore the processes responsible for the seasonal EKE fluctuations, it is relevant to first clarify whether the EKE signals obtained in Figure 3b are representative vertically in the water column. To address this issue, we use the QSCAT run output and calculate the EKE time series as a function of depth, $E(t, z)$, in the region of 125°E–150°E and 2.5°N–10°N. Figure 5 (blue line) shows the mean EKE level as a function of depth normalized by its surface value: $\langle E(t, z) \rangle / \langle E(t, 0) \rangle$, where $\langle \rangle$ denotes temporal averaging. The result reveals that the regional EKE level reduces rapidly with increasing depth. At the 200 m depth, the EKE level is only 17% that at the surface. Also shown in Figure 5 (red line) is a measure of coherence of the EKE time series at depth with respect to the surface time series, defined by:

$$C(z) \equiv 1 - \frac{\langle [E(t, z) - r(z)E(t, 0)]^2 \rangle}{\langle E^2(t, z) \rangle} \quad (3)$$

where $r(z) \equiv \langle E(t, z)E(t, 0) \rangle / \langle E^2(t, 0) \rangle$ is a regression coefficient. Physically, $C(z)$ gives the ratio of the $E(t, z)$ variance that is coherent with respect to $E(t, 0)$. With $C(z)$ exceeding 0.85 at all depth, the result of Figure 5 indicates that the temporal variability of EKE behaves similarly at depth as that at surface. Given

variations and their linear correlation coefficient reaches 0.63. This comparison indicates that the QSCAT run is capable of simulating well the temporal variability of eddy activity in the region of our interest. Notice that there exists a tendency for the EKE signals in both Figures 3a and 3b to peak in summer, although large interannual changes often obscure this seasonal tendency.

In order to clarify the frequency content of the time-varying signals contributing to the EKE time series shown in Figure 3, we plot in Figure 4 the variance-preserved power spectra of the AVISO and QSCAT surface geostrophic velocity anomalies in the area of 125°E–150°E and 2.5°N–10°N, respectively. Aside from the spectral peaks at the annual and semiannual periods (frequency = 2.74×10^{-3} and

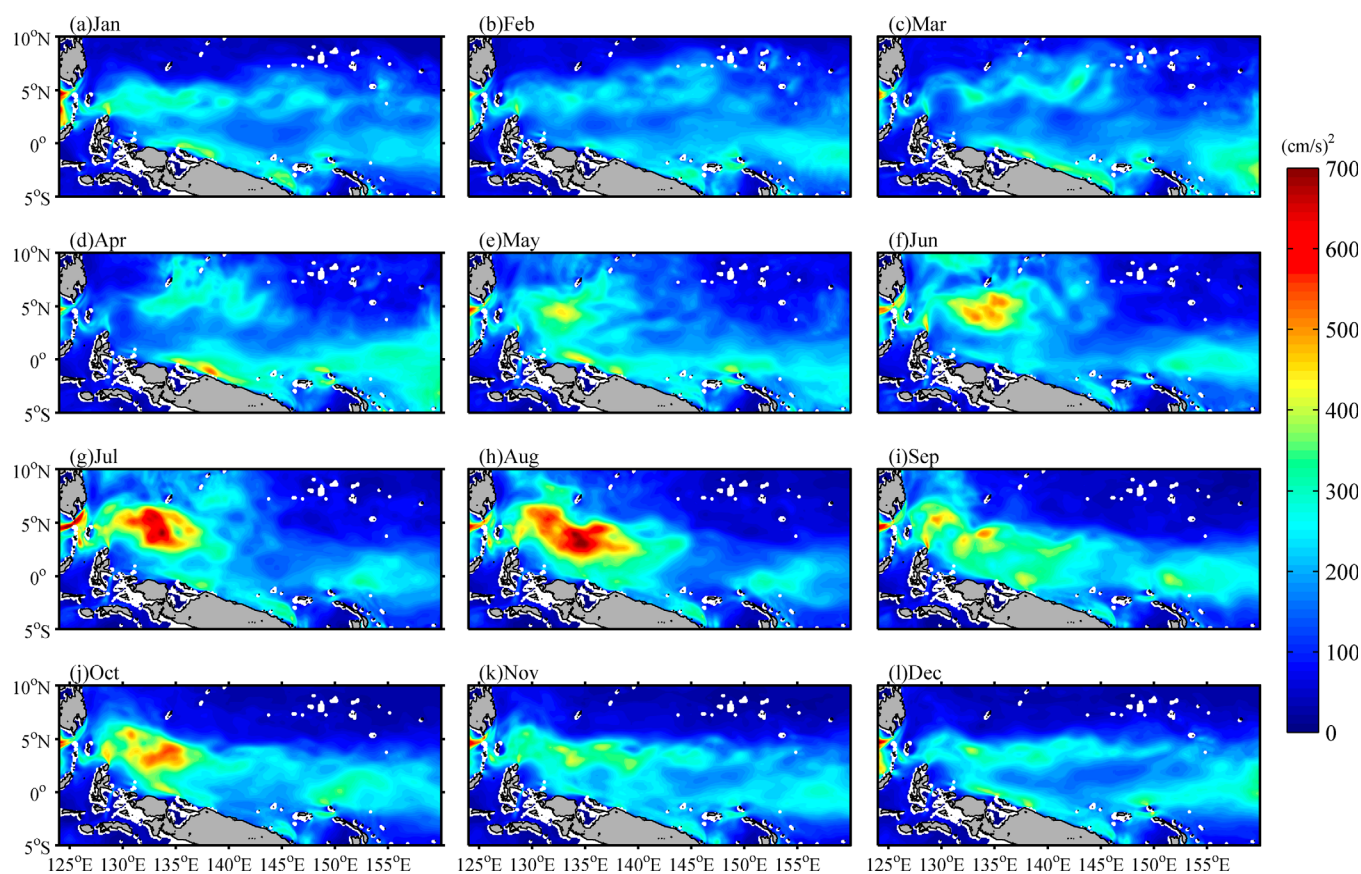


Figure 6. Monthly mean EKE distributions in the upper 200 m layer. Here EKE is calculated from the 150 day high-pass filtered velocity data from the QSCAT run of 2000–2008.

this vertical coherence and confinement, our analyses below focus on the seasonal EKE signals that are averaged in the upper 200 m layer.

Figure 6 shows the monthly mean mesoscale EKE distributions in the western tropical Pacific evaluated from the QSCAT run of 2000–2008. Here the mesoscale EKE values are averaged in the upper 200 m layer

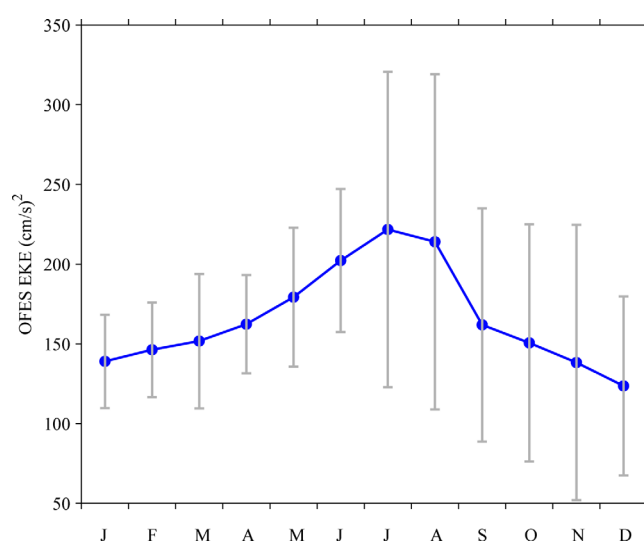


Figure 7. EKE time series averaged in the upper 200 m layer in 125°E–150°E, 2.5°N–10°N as a function of months. Here EKE is calculated using 150 day high-pass filtered velocity data from year 2000 to 2008. Vertical bars indicate standard deviations.

and, as defined in equation (2), the high-pass filtered u'' and v'' data are used to evaluate the EKE values. Starting from May, an elevated mesoscale EKE signal appears in the region south-southwest off Palau (Figure 6e). It increases in intensity progressively as the season marches on. After peaking around July/August, the mesoscale EKE signal south-southwest off Palau weakens and, during the winter months of December–March, it attains an energy level indistinguishable from the other parts of the NECC.

In Figure 7, we plot the mesoscale EKE time series in the 125°E–150°E and, 2.5°N–10°N region as a function of calendar months. With a maximum ($\sim 220 \text{ cm}^2/\text{s}^2$) in July and a minimum ($\sim 125 \text{ cm}^2/\text{s}^2$) in December, the

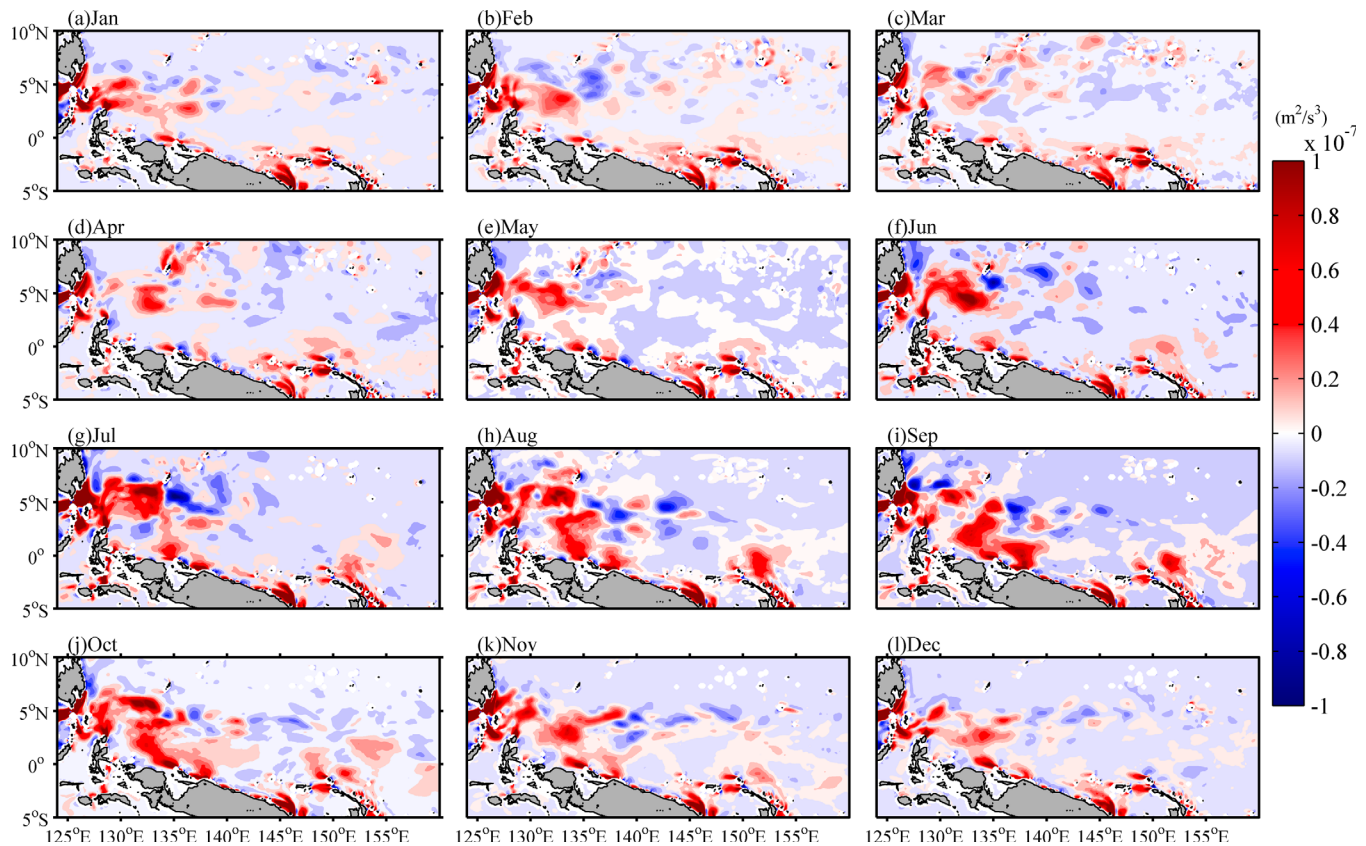


Figure 8. Monthly mean barotropic conversion rate (BTR) distribution from the QSCAT run. See equation (4) for the definition of BTR.

seasonality of the mesoscale EKE field in this broad region is clearly dominated by the local EKE signals emerging in the region south-southwest of Palau. Accompanied by their elevated mesoscale EKE levels, the standard deviations are greater in the latter half of a year with maxima in July/August and smaller in the first half of a year with minima in January/February (see vertical bars in Figure 7).

5. Processes Governing the Seasonal EKE Variability

In order to clarify the processes governing the seasonal variations of mesoscale EKE in the region of our interest, we evaluate the barotropic and baroclinic eddy energy conversion rates with the use of the QSCAT run output. Here the two conversion rates are defined as follows:

$$\text{barotropic conversion rate} = - \left(u'' u'' \frac{\partial \tilde{u}}{\partial x} + u'' v'' \left(\frac{\partial \tilde{v}}{\partial x} + \frac{\partial \tilde{u}}{\partial y} \right) + v'' v'' \frac{\partial \tilde{v}}{\partial y} \right) \quad (4)$$

and

$$\text{baroclinic conversion rate} = - \left(\frac{g}{\rho_0} \rho'' w'' \right) \quad (5)$$

where u'' and v'' are the high-pass filtered horizontal velocity anomalies, and \tilde{u} and \tilde{v} denote the slowly varying background horizontal currents (including time-mean flows) with time scales longer than 150 days. Similarly, ρ'' and w'' are the 150 day, high-pass filtered potential density and vertical velocity anomalies, and g and ρ_0 are the gravity constant and the background potential density ($\rho_0 = 1025 \text{ kg/m}^3$), respectively. Physically, equation (4) indicates the kinetic energy transformation from the mean flow to eddies, and a positive barotropic conversion rate suggests the barotropic instability of the background circulation. Equation (5) represents the potential energy conversion from the mean potential energy field to eddy potential

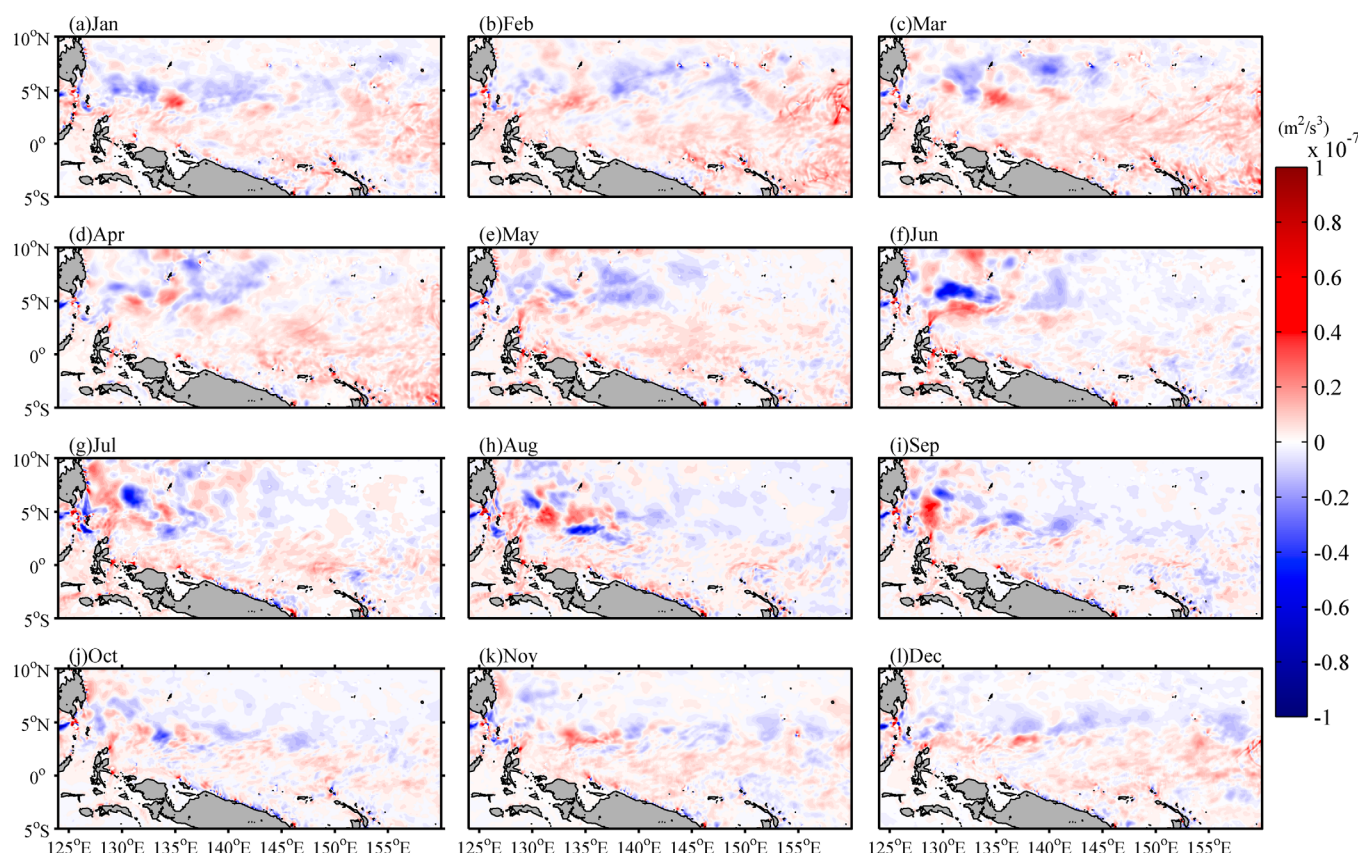


Figure 9. Monthly mean baroclinic conversion rate (BCR) distribution from the QSCAT run. See equation (5) for the definition of BCR.

energy field, and a positive baroclinic conversion rate hints the baroclinic instability of the background circulation.

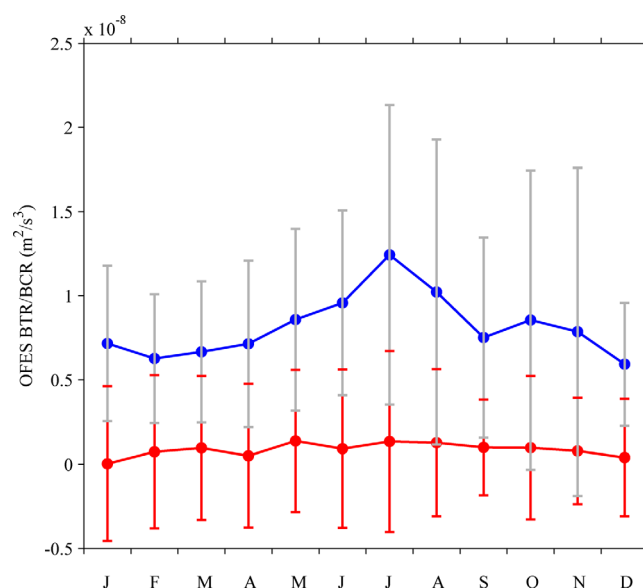


Figure 10. Time series of barotropic (blue) and baroclinic (red) conversion rate averaged in the upper 200 m layer in 125°E–150°E, 2.5°N–10°N as a function of months. Vertical bars indicate standard deviations.

Figure 8 shows the monthly distributions of the barotropic conversion rate averaged in the upper 200 m layer in the western equatorial Pacific. Starting from April, it is interesting to note that a positive barotropic conversion rate signal appears south-southwest off Palau. This signal increases in magnitude progressively until July and weakens steadily after August. This seasonal signal of barotropic conversion rate matches favorably to the seasonal evolution in mesoscale EKE signals in the region south-southwest off Palau (recall Figure 6). The importance of barotropic conversion in generating mesoscale eddies along the surface layer NECC has been similarly noted in a recent study by Chen *et al.* [2015]. From Figure 8, it is also interesting to note that the region north of the New Guinea is another area where the barotropic conversion rate exhibits a clear seasonal modulation. Specifically, an elevated barotropic conversion

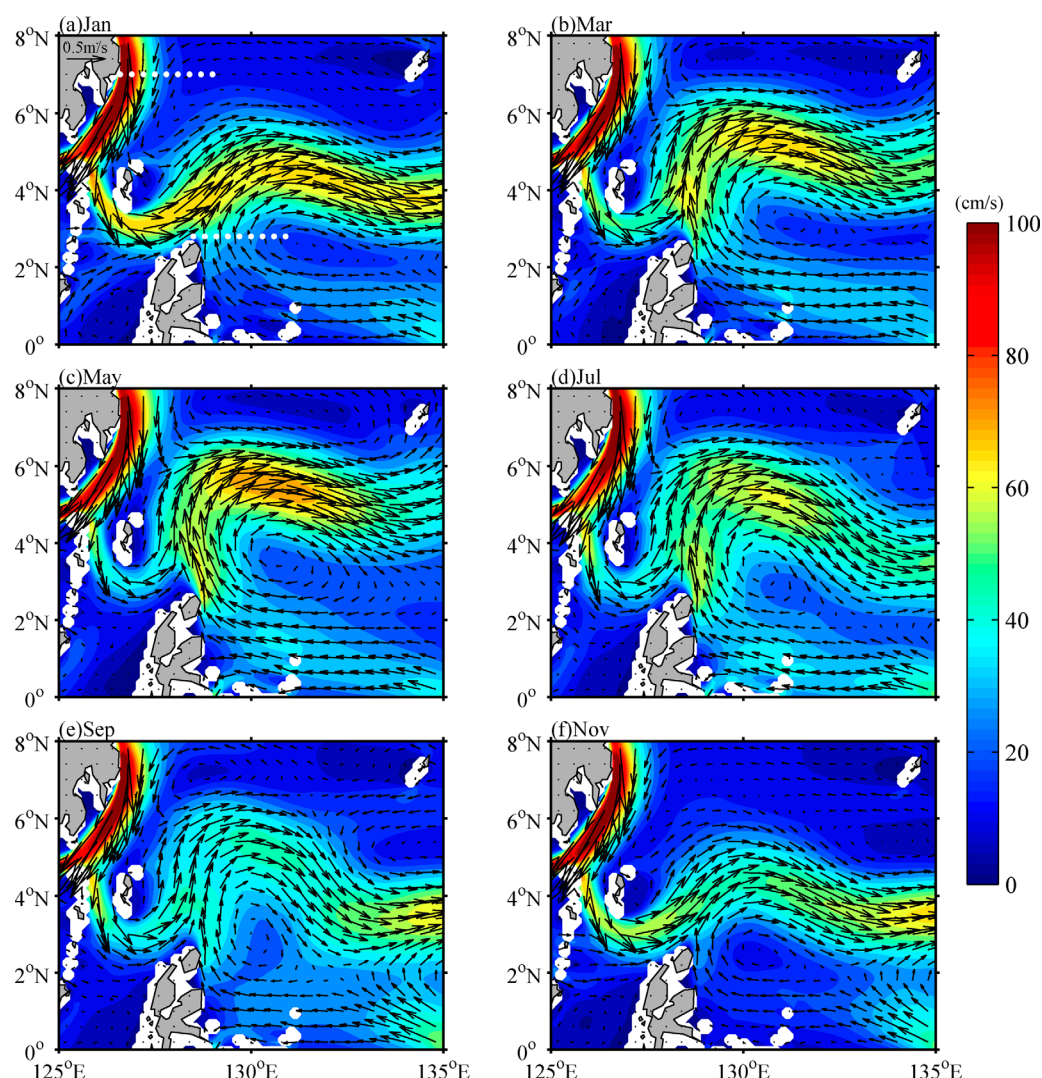


Figure 11. Bimonthly velocity vector and magnitude (in color) distributions in the upper 200 m layer of the western tropical Pacific. Here the upper ocean velocities are based on the 150 day low-pass filtered QSCAT run output (that includes the time-mean circulation).

rate signal appears near 135°E in July along the New Guinea coast; it intensifies and expands along the coast during August and September and weakens subsequently after October. A look at Figure 6 reveals the corresponding seasonal evolution in the mesoscale EKE field along the New Guinea coast.

In Figure 9, we plot the monthly baroclinic conversion rate distributions in the western tropical Pacific. The rates are again averaged in the upper 200 m layer. Compared to the barotropic conversion rates shown in Figure 8, the baroclinic conversion rates in the region have a much smaller amplitude and there appears no clear seasonal variation. This lack of seasonal variation can be confirmed if we plot as a time series the baroclinic conversion rate averaged in the region of 125°E–150°E, 2.5°N–10°N (see the red line in Figure 10). In contrast, the region-averaged barotropic conversion rate, as shown by the blue line in Figure 10, reveals a clear annual cycle that has a similar seasonality as that of the mesoscale EKE (cf. Figure 7). The energetic analysis results shown above clearly demonstrate that the barotropic instability associated with the horizontal shear of the slowly varying background circulation is responsible for the seasonal mesoscale EKE modulations detected in the western tropical Pacific.

6. Discussion and Summary

In order to understand the cause underlying the seasonally varying barotropic conversion occurring in the western tropical Pacific, we examine the upper ocean circulation changes in the region with the prominent

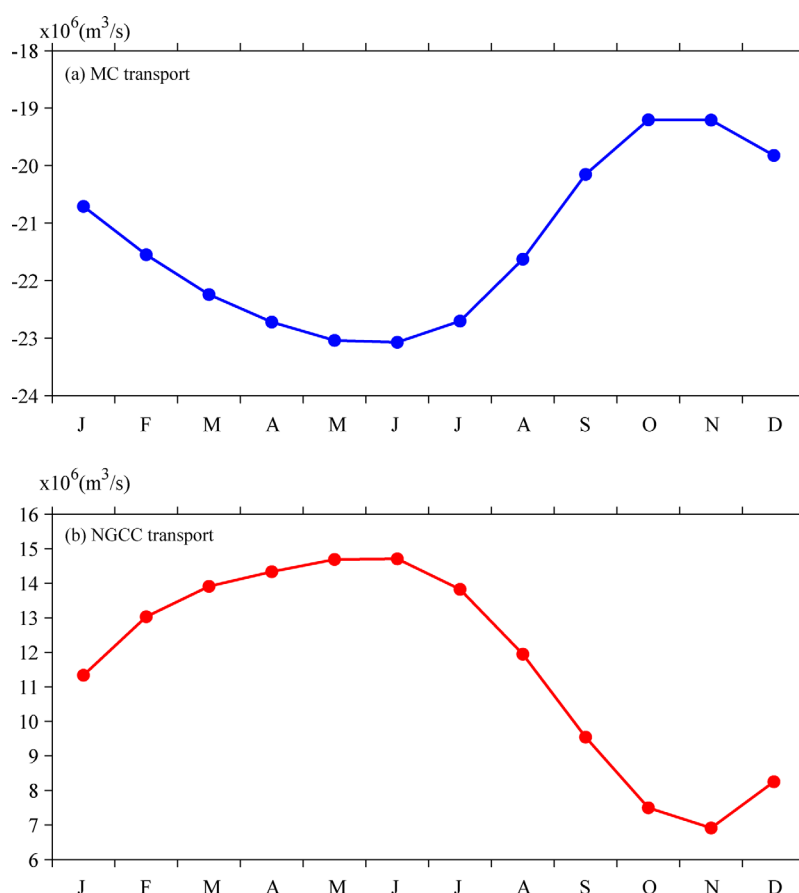


Figure 12. Transport time series of (a) the MC across 7°N from 126.5°E to 129°E and (b) the NGCC across 2.8°N from 128.5°E to 131°E in the upper 200 m layer. See Figure 11a for the cross sections.

seasonal changes in barotropic conversion rate. Figure 11 shows the monthly velocity vector and magnitude (color shades) fields averaged in the upper 200 m layer. Although difficult to discern visually from Figure 11, the equatorward-flowing MC across 7°N off the Philippine coast is the strongest (with a transport of ~23 Sv) in June and weakest (~19 Sv) in October (see Figure 12a). Concurrent with the seasonally evolving MC east of the Mindanao Island, the northward-flowing NGCC east of the Halmahera Island exhibits a very similar seasonal change in its transport: a maximum of ~15 Sv in June and a minimum of ~7 Sv in November (Figure 12b). The combined changes of MC and NGCC transport affect the NECC significantly. As depicted in Figure 11, the path of the NECC is mostly aligned zonally during January to March. It starts to meander more prominently after May, following the seasonal strengthening of the MC and NGCC. The meandering of NECC

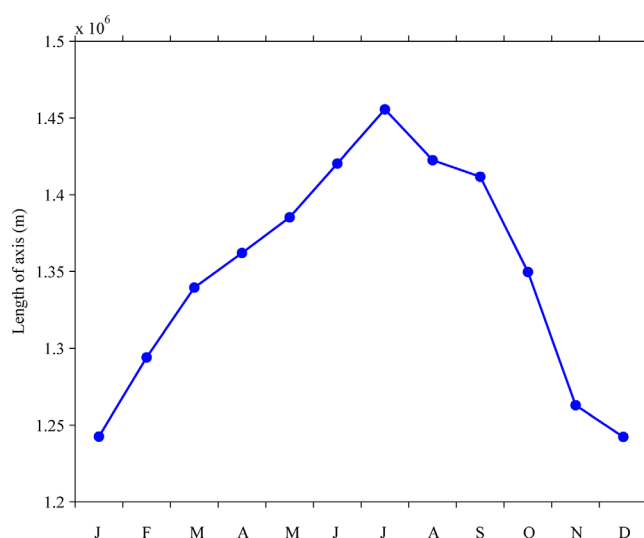


Figure 13. Time series of the path length of the NECC (defined by its maximum speed axis) in the upper 200 m layer from 125.7°E off the Philippine to 135°E north of the New Guinea. See Figure 11 for the velocity vector and magnitude distributions used for the path length estimations.

As depicted in Figure 11, the path of the NECC is mostly aligned zonally during January to March. It starts to meander more prominently after May, following the seasonal strengthening of the MC and NGCC. The meandering of NECC

appears to reach its maximum amplitude in July, 1 month after the transports of MC and NGCC attain their seasonal maxima.

The seasonal changes of the NECC meandering can be evaluated quantitatively by integrating the path of the NECC (defined by the location of its maximum speed) from 125.7°E east of the Mindanao Island to 135°E southeast of Palau. As shown in Figure 13, the NECC path length has a maximum in July when the NECC has the most undulating path and a minimum in December when the NECC takes a weakly meandering path. Dynamically, a longer integrated path signifies greater curvatures, or nonlinear shears, in the horizontal flow field and a large source of mean kinetic energy extractable for barotropic instability. The correspondence among the time series in Figures 7, 10, and 13 indicates that the seasonal EKE variability detected along the NECC is caused by barotropic conversion that fluctuates seasonally in connection with the intensification of the NECC meandering. Originating from the upstream MC, as well as being enhanced by the NGCC east of the Halmahera Island, the seasonal NECC variability is attributable to the changes of the MC and NGCC that have their respective origins in the wind-driven tropical gyres of the North and South Pacific.

In concluding this study, it is worth emphasizing that the NECC constitutes a strong meridional property boundary between water masses originating from the North and South Pacific Oceans [e.g., Qiu and Joyce, 1992; Gouriou and Toole, 1993]. The seasonally varying eddy variability in the western tropical Pacific can potentially affect the regional mixing of water properties of different origins, as well as the water properties carried eastward by the NECC and transported westward into the eastern Indian Ocean through the Indonesian Throughflow [e.g., Gordon and Fine, 1996]. Although we have examined in this study the dynamical cause underlying the seasonal eddy variability, future studies are needed to clarify how this eddy variability and its seasonal modulation could impact upon the water property changes in the tropical Pacific and Indian Oceans.

Acknowledgments

We acknowledge the AVISO for providing SSH anomalies data (<http://www.aviso.oceanobs.com/en>). The OFES simulation was conducted on the Earth Simulator under the support of JAMSTEC. The QSCAT simulation used in our study is obtained from APDRC, University of Hawaii (<http://apdrc.soest.hawaii.edu>). This study is supported by the Strategic Priority Research Program of the Chinese Academy of Sciences (grant XDA11010103 and XDA11010203), the National Natural Science Foundation of China (grant 41176024 and 41176023), the National Basic Research Program of China (grant 2014CB745001), the Open Project Program of State Key Laboratory of Tropical Oceanography (grant LTOZZ1501), the CAS/SAFEA International Partnership Program for Creative Research Teams and the China Scholarship Council.

References

- Boyer, T. P., and S. Levitus (1997), *Objective Analyses of Temperature and Salinity for the World Ocean on a 1/4° Grid*, NOAA Atlas NESDIS, vol. 11, Natl. Oceanic and Atmos. Admin., Silver Spring, Md.
- Chen, L., Y. Jia, and Q. Liu (2015), Mesoscale eddies in the Mindanao Dome region, *J. Oceanogr.*, *71*, 133–140, doi:10.1007/s10872-014-0255-3.
- Chen, Z., and L. Wu (2011), Dynamics of the seasonal variation of the North Equatorial Current bifurcation, *J. Geophys. Res.*, *116*, C02018, doi:10.1029/2010JC006664.
- Gordon, A. L., and R. A. Fine (1996), Pathways of water between the Pacific and Indian oceans in the Indonesian seas, *Nature*, *379*(6561), 146–149.
- Gouriou, Y., and J. Toole (1993), Mean circulation of the upper layers of the western equatorial Pacific Ocean, *J. Geophys. Res.*, *98*, 22,495–22,520, doi:10.1029/93JC02513.
- Heron, S. F., E. J. Metzger, and W. J. Skirving (2006), Seasonal variations of the ocean surface circulation in the vicinity of Palau, *J. Oceanogr.*, *62*(4), 413–426, doi:10.1007/s10872-006-0065-3.
- Hsin, Y.-C., and B. Qiu (2012a), Seasonal fluctuations of the surface North Equatorial Countercurrent (NECC) across the Pacific basin, *J. Geophys. Res.*, *117*, C06001, doi:10.1029/2011JC007794.
- Hsin, Y.-C., and B. Qiu (2012b), The impact of Eastern-Pacific versus Central-Pacific El Niño on the North Equatorial Countercurrent in the Pacific Ocean, *J. Geophys. Res.*, *117*, C11017, doi:10.1029/2012JC008362.
- Kalnay, E., et al. (1996), The NCEP/NCAR 40-year reanalysis project, *Bull. Am. Meteorol. Soc.*, *77*, 437–471, doi:10.1175/1520-0477(1996)077<0437:TNYRP>2.0.CO;2.
- Kashino, Y., E. Firing, P. Hacker, A. Sulaiman, and Lukiyanto (2001), Currents in the Celebes and Maluku Seas, February 1999, *Geophys. Res. Lett.*, *28*, 1263–1266.
- Kashino, Y., A. Ishida, and Y. Kuroda (2005), Variability of the Mindanao Current: Mooring observation results, *Geophys. Res. Lett.*, *32*, L18611, doi:10.1029/2005GL023880.
- Kashino, Y., A. Atmadipoera, Y. Kuroda, and Lukiyanto (2013), Observed features of the Halmahera and Mindanao Eddies, *J. Geophys. Res. Oceans*, *118*, 6543–6560, doi:10.1002/2013JC009207.
- Kim, Y. Y., T. Qu, T. Jensen, T. Miyama, H. Mitsudera, H.-W. Kang, and A. Ishida (2004), Seasonal and interannual variations of the North Equatorial Current bifurcation in a high-resolution OGCM, *J. Geophys. Res.*, *109*, C03040, doi:10.1029/2003JC002013.
- Le Traon, P.-Y., and F. Ogor (1998), ERS-1/2 orbit improvement using TOPEX/Poseidon: The 2 cm challenge, *J. Geophys. Res.*, *103*, 8045–8057.
- Le Traon, P.-Y., F. Nadal, and N. Ducet (1998), An improved mapping method of multisatellite altimeter data, *J. Atmos. Oceanic Technol.*, *15*, 522–534.
- Lukas, R., E. Firing, P. Hacker, P. L. Richardson, C. A. Collins, R. Fine, and R. Gammon (1991), Observations of the Mindanao Current during the Western Equatorial Pacific Ocean Circulation Study, *J. Geophys. Res.*, *96*, 7089–7104.
- Masumoto, Y., and T. Yamagata (1991), Response of the western tropical Pacific to the Asian winter monsoon: The generation of the Mindanao Dome, *J. Phys. Oceanogr.*, *21*, 1386–1398.
- Masumoto, Y., et al. (2004), A fifty-year eddy-resolving simulation of the world ocean: Preliminary outcomes of OFES (OGCM for the Earth Simulator), *J. Earth Simulator*, *1*, 35–56.

- Nitani, H. (1972), Beginning of the Kuroshio, in *Kuroshio: Its Physical Aspects*, edited by H. Stommel and K. Yoshida, pp. 129–163, Univ. of Tokyo Press, Tokyo.
- Qiu, B., and S. Chen (2010), Interannual-to-decadal variability in the bifurcation of the North Equatorial Current off the Philippines, *J. Phys. Oceanogr.*, *40*, 2525–2538.
- Qiu, B., and T. M. Joyce (1992), Interannual variability in the mid- and low-latitude western North Pacific, *J. Phys. Oceanogr.*, *22*, 1062–1079.
- Qiu, B., and R. Lukas (1996), Seasonal and interannual variability of the North Equatorial Current, the Mindanao Current and the Kuroshio along the Pacific western boundary, *J. Geophys. Res.*, *101*, 12,315–12,330.
- Reverdin, G., C. Frankignoul, E. Kestenare, and M. J. McPhaden (1994), Seasonal variability in the surface currents of the equatorial Pacific, *J. Geophys. Res.*, *99*, 20,323–20,344, doi:10.1029/94JC01477.
- Sasaki, H., M. Nonaka, Y. Masumoto, Y. Sasai, H. Uehara, and H. Sakuma (2008), An eddy-resolving hindcast simulation of the quasiglobal ocean from 1950 to 2003 on the Earth simulator, in *High Resolution Numerical Modeling of the Atmosphere and Ocean*, edited by K. Hamilton and W. Ohfuchi, pp. 157–185, Springer, N. Y.
- Tozuka, T., T. Kagimoto, Y. Masumoto, and T. Yamagata (2002), Simulated multiscale variations in the western tropical Pacific: The Mindanao Dome revisited, *J. Phys. Oceanogr.*, *32*, 1338–1358, doi:10.1175/1520-0485(2002)032<1338:SMVITW>2.0.CO;2.
- Ueki, I., Y. Kashino, and Y. Kuroda (2003), Observation of current variations off the New Guinea coast including the 1997–1998 El Niño period and their relationship with Sverdrup transport, *J. Geophys. Res.*, *108*(C7), 3243, doi:10.1029/2002JC001611.
- Wyrtki, K. (1974), Sea level and the seasonal fluctuations of the equatorial currents in the western Pacific Ocean, *J. Phys. Oceanogr.*, *4*(1), 91–103, doi:10.1175/1520-0485(1974)004<0091:SLATSF>2.0.CO;2.
- Wyrtki, K., and R. Kendall (1967), Transports of the Pacific equatorial countercurrent, *J. Geophys. Res.*, *72*, 2073–2076, doi:10.1029/JZ072i008p02073.